Green Chemistry

PAPER

View Article Online
View Journal | View Issue

Cite this: *Green Chem.*, 2021, **23**, 5724

Ethylenediamine series as additives to control the morphology of magnetite nanoparticles†

Laura Norfolk, *[a] Klaudia Kapusta,[a] David Cooke [b] and Sarah Staniland [a]

Magnetite nanoparticles play a key role in the nano-industry, with crucial importance in the developing nanomedicine sector. Such particles must be homogeneous, with a consistent shape and size, due to the growing need to tailor particles to more defined faceted morphologies. Here an ethylenediamine series (H_2N-(–CH_2CH_2N–)$_n$$H_2$, n = 2 (DETA), 3 (TETA), 4 (TEPA), and 5 (PEHA)), of additives have been successfully used to control the morphology of nanomagnetite produced *via* a green ambient co-precipitation method. Whilst DETA showed less control, TETA, TEPA and PEHA mediated the near universal synthesis of faceted particles (91–97%) suggesting a near pure octahedral population (compared to only 6% of control particles). The particle size was ≈ 22 nm for all the samples and was not affected by the addition of additives. Computational molecular dynamic modelling shows the binding to the octahedral [111] face to be preferred for all additives with binding to the [100] face unfavourable for TETA, TEPA and PEHA, showing a preference to bind and direct an octahedral morphology for these 3 additives. This is further explained by the increased numbers of interactions of the longer additives with the [111] surface through O and Fe in the magnetite surface bonding to H and N in the additive which is better able to lie flat on the [111] surface. An optimum concentration of a 1 : 125 additive : iron ion ratio was determined which shows that a relatively small quantity of a cheap, organic bioinspired amine-rich additive can have a massive impact on the morphological quality of the magnetite nanoparticles. This powerful, additive-directed, green synthesis approach could be universally applied to a vast range of nanomaterial syntheses to great impact.

Received 2nd May 2021,
Accepted 24th June 2021

DOI: 10.1039/d1gc01539g

rsc.li/greenchem

Introduction

In recent years, magnetite (Fe_3O_4) nanoparticles (MNPs) have been extensively researched for their widespread applications in industry such as their use in magnetic inks[1] and carbon capture,[2] and importantly, their wide potential in the biomedical industry.[3–6] Their use is being realised as Magnetic Resonance Imaging (MRI) contrast agents,[7] drug delivery systems,[8] and hyperthermic cancer treatments.[9]

For any application, control over the size, shape, composition, mono-dispersity and reproducibility is beneficial, but it is critical with MNPs for nanomedicine, with the ability to precisely tune the particles to specific requirements – a much sought-after feature of production. Monodispersity is key to ensure uniform, consistent and predicable magnetic properties, anatomical uptake, anatomical distribution and therapeutic dosing/effects.

Control over the size is essential (1) to understand the surface area and thus dosing levels; (2) to direct the anatomical location (as different sized MNPs concentrate in different parts of the body); and (3) to tune the magnetic response, with smaller MNPs exhibiting superparamagnetism with profound effects on hyperthermic heating.[10]

Control over the shape also varies the properties of the nanomedicine. Due to particle nuclei formation requiring a low surface area to volume ratio, the smallest MNPs will be spherical. While being highly dependent on the reaction conditions, as the MNP grows, magnetite's low index crystal faces (γ[111] < γ[100] < γ[110]) tend to be favoured in the final crystal form.[11] As such, a typical equilibrium morphology is cubo-octahedral (a truncated cube which appears spherical) incorporating a reduced surface area and the most stable [111] and [100] facets.[12] However, more faceted (non-spherical) MNPs have been shown to offer the most promise across a range of nanomedicines. For example, cubic nanoparticles have been found to be preferable for contrast agents compared to spherical particles (with similar volumes),[13,14] while angular "nanoflower" shaped MNPs have been found to have higher hyperthermic heating compared to spherical MNPs.[15,16] This is thought to be due to the physical effect of the points and edges.[15,16] As such, the demand for non-spherical faceted

[a]*Department of Chemistry, The University of Sheffield, Dainton Building, Brook Hill, Sheffield, S3 7HF, UK. E-mail: s.s.staniland@sheffield.ac.uk*
[b]*Department of Chemical Sciences, The University of Huddersfield, Huddersfield, HD1 3DH, UK*

†Electronic supplementary information (ESI) available. See DOI: 10.1039/d1gc01539g

MNPs in the biomedical industry is on the rise with synthetic control over the size, shape, and crystal quality of particles being crucial.

Whilst many syntheses exist to carefully tailor the morphology (shape and size) of MNPs, most of these techniques require environmentally unsustainable reaction conditions, increasing the negative environmental impact of the syntheses. The manufacture of cubic or nanoflower MNPs currently requires high temperature,[17,18] alongside a range of organic reagents, or microwaves,[19] while octahedral MNPs require an elevated temperature to allow the kinetically favoured [111] facet to dominate.[20] These synthetic routes are not green, demonstrating a general problem with inorganic nanomaterial synthesis: precisely faceted nanomaterial production requires highly wasteful and less environmentally friendly synthesis.

Magnetite can be easily synthesized on a large scale using a room-temperature co-precipitation (RTCP) reaction (Fig. 1a). The addition of a base such as NaOH, KOH, or Et_4NOH to an aqueous solution of ferric and ferrous iron under an inert atmosphere at room temperature produces iron oxides without the use of toxic solvents/reagents.[21] This is a fast and straightforward green synthesis, with no use of high energy processes such as heating or vacuum pressure allowing for large volumes of particles to be produced. The disadvantage of this green synthesis is that there is very little control over the final product, with a broad size distribution (5–40 nm) of an undefined/pseudo-spherical shape with little opportunity to tailor the morphology.

Within the green chemistry remit (ambient conditions), some control can be offered by changing the reaction conditions, using such systems as micro-[22] and milli-fluidic flow synthesis[23] or pH-regulated synthesis;[24] however, these methods are not currently scalable to large-scale production and offer less control over the particle shape.

The use of additives in a green RTCP is an established method to offer control over nanoparticle synthesis.[25] Grafted co-polymer additives have been used to control the size of magnetite MNPs[26] while there are many examples of green/natural additives being used such as unrefined seaweed[27] and plant leaf extracts in the synthesis of MNPs,[28–30] as well as citrate,[31] oxalic acid[32] and chitosan.[33] Green additives such as fruit juice and sea buckthorn have also been used to control the size of gold[34] and silver[35,36] nanoparticles. However, all these examples produce spherical particles or particles of undefined morphology. Clearly, shape is more difficult to control with additive synthesis, with the green synthesis of tailored faceted MNPs offering a greater challenge.

Highly uniform, morphologically controlled MNPs are observed in nature, for example within magnetotactic bacteria. These unique bacteria foster the ability to precisely control the synthesis of MNPs using magnetosome membrane specific (Mms) biomineralisation proteins such as Mms6[37–41] and MmsF.[42] This has translated to the successful use of several Mms proteins as biological additives to mediate the formation of enhanced MNPs in simple RTCP syntheses. Purified Mms6, MmsF and an MmsF protein mimic[60] have been used *in vitro* to control particle formation in RTCP reactions, with increased control over the size (Mms6) and morphology (MmsF) and magnetite mineral purity (both) compared to protein free reactions.[38,39,41,42,60]

Recently, by screening an (Adhiron) affimer protein phage-display library against cubic [100] magnetite (labelled MIA (Magnetite Interacting Adhiron)), we identified a protein additive that specifically directs the formation of cubic MNPs. The resulting MIAs were found to contain high levels of basic residues, particularly lysine.[43] Molecular dynamics simulations showed the amino acid lysine to have the lowest adsorption energy to the magnetite [100] surface through amine inter-

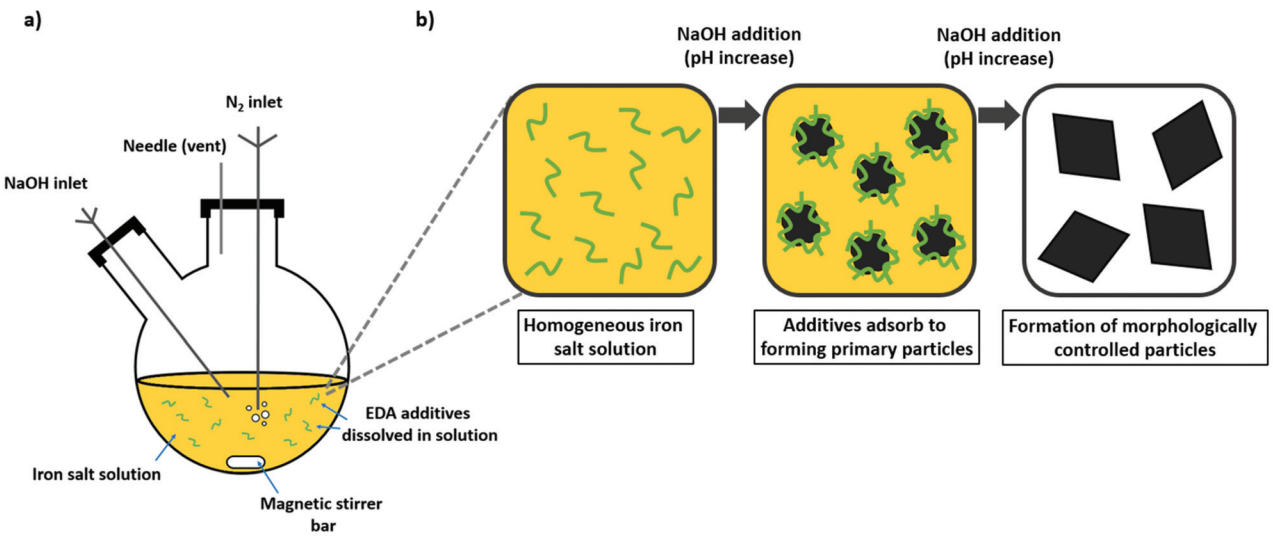

Fig. 1 (a) Schematic of the experimental setup for an RTCP reaction containing an organic additive or protein *in vitro*. (b) The reaction progression on addition of NaOH is shown, with the role of additives adsorbing to the surface of forming primary particles, and finally the production of morphologically controlled particles.

actions with the surface.[43] Adsorption of MIA additives to the magnetite [100] surface of a developing crystal results in stabilizing and propagating that surface allowing it to dominant the final (cubic) particle structure. This was seen in RTCP reactions where cubic MNPs were formed when mediated by an MIA protein additive, a morphology previously only accessible using organic solvents and high-temperature methods. From this work, we saw that the amine rich additive controlled the MNP morphology through adsorption to the magnetite surface.[43]

Whilst complex proteins are green additives capable of specific crystal face binding to control morphology, they are very expensive to produce compared to the other additives cited above. For example, a commonly used arginine based synthetic protein costs £49 per mg,[44] with more bespoke and membrane proteins costing multiple times more. In this study, we take a systematic approach to understand morphology controlling protein additives and use this to develop cheaper bioinspired additives to mediate the RTCP of faceted MNPs.

We identify the importance of amine groups for interacting with magnetite surfaces to control their morphology. In this study, we screen an ethylenediamine series (amines linked with aliphatic CH_2CH_2 spacers of various lengths) as bioinspired additives for RTCP of faceted MNPs. Ethylenediamines are small, simple and cheap additives for a green RTCP synthesis that pose a more realistic commercially viable proposition for scale-up and green manufacture at a millionth of the cost of a protein additive (tetraethylenepentamine is £55.30 per kg (ref. 45)), demonstrating that this method could be used for the green production of magnetite on an industrially viable scale.

If the nanomaterial industries, particularly biomedical, are to continue to expand and precisely faceted MNPs are required on a larger scale, it is critical to develop synthetic methods that offer substantial reductions in energy usage and manufacturing carbon footprint whilst still offering precise control over the nanomaterial properties. Here we demonstrate that ethylenediamine additives in green RTCP have the ability to control morphology with the precision of proteins at a fraction of the cost.

Experimental

Materials and methods

All reactions were carried out under an inert atmosphere of N_2, and all solutions were sparged with N_2 for 30 minutes prior to use. Ultrapure Milli-Q water (Merck Milli-Q integral purification system) was used. All reagents were purchased from Sigma Aldrich.

Room temperature co-precipitation

Iron(II) sulphate (111 mg, 0.4 mmol) and iron(III) sulphate (179 mg, 0.3 mmol) were dissolved in N_2 sparged Milli-Q (20 mL) in a two-neck round bottomed flask. A set amount of the additive was added to the reaction mixture and left to stir for 5 minutes to ensure dissolution of the additive and iron salts under an N_2 atmosphere. N_2 sparged 0.5 mol NaOH (8 mL) was added at a rate of 50 μL a minute with stirring, for a total of 160 minutes using a Harvard Apparatus 11 plus syringe pump driver. The reaction was left to age for an hour under the inert atmosphere. The reaction mixture was then magnetically separated, washed five times with sparged Milli-Q to remove any non-magnetic iron oxide by-products, and the particles dried in a 40 °C vacuum oven overnight. All reactions produced a high yield of particles (>85%).

Characterisation

Transmission electron microscopy (TEM). 10 μL of a 1 mg ml^{-1} suspension of nanoparticles in hexane was dropped onto a carbon coating copper TEM grid and allowed to dry down. Grids were imaged using an FEI Technai G2 Spirit electron microscope and the TEM images were analysed using the ImageJ software. >200 particles per sample were randomly selected and measured (see ESI S1 and S2† for the full protocol of sample analysis). For HRTEM and selected-area electron diffraction, an FEI Titan microscope was used.

X-ray diffraction (XRD). The XRD data were collected by the analysis of dry iron oxide nanoparticles in a Bruker D8 powder diffractometer. The diffraction images were collected in 0.022-degree increments from 20 to 80 degrees, with a fixed wavelength at λ = 1.54178 Å from a Cu Kα X-ray source.

Fourier-transform infrared spectrometry (FTIR). FTIR was performed on a small quantity (5–10 mg) of dry iron oxide nanoparticles using a PerkinElmer FTIR and Golden Gate Diamond ATR spectrometer. The particles were dispersed in a 0.05 M solution of TEPA in ultrapure Milli-Q and sonicated for 10 minutes. The solution pH was adjusted to the desired pH using 0.5 M HCl/0.5 M NaOH and rotated for 1 hour using a Lab net Mini Labroller. The particles were then magnetically separated, washed with pH adjusted Milli-Q (adjusted to the same desired pH), and dried overnight in a vacuum dessicator. Data collection and analysis were performed using Spectrum 10, with scans being made between 450 and 4000 cm^{-1}. Baseline correction was performed on all the spectra.

Thermal gravimetric analysis (TGA). To ascertain the binding of organic material to iron oxide nanoparticles, a small amount (10–20 mg) of particles were washed with ethanol and acetone to remove any residual surface organic debris and dried in a vacuum oven. The cleaned particles were then dispersed in a 0.05 M solution of TEPA in ultrapure Milli-Q and sonicated for 10 minutes. The solution pH was adjusted to ~pH 7 using 0.5 M HCl and rotated for 1 hour using a Lab net Mini Labroller. The particles were then magnetically separated and washed using ultrapure water to remove excess unbound amine and dried overnight in a vacuum desiccator.

TGA was performed on these dry particles between 20 and 800 °C at a heating rate of 10 °C per minute under a 2/3 N_2 and 1/3 O_2 atmosphere.

Computational modelling

The computational study used an approach similar to our previous study of magnetite surfaces.[43] The DL_POLY Classic

code[46] using the Generalised AMBER Force Field (GAFF)[47] for the ethylenediamine molecules, a modified version of CLAYFF for magnetite[48,49] with standard, Lorentz–Berthelot[50,51] mixing rules, was used to define the interaction between the two force-fields. Applying this approach to describe the interface between two very different media is not normally advisable and its reliability should be tested before production runs are performed.[52] However the similarity in form of the two force-fields and the partial charges associated with the atoms on both sides of the interface meant that our tests showed that the approach adequately described the interface between magnetite and a range of simple organic molecules.[53] The approach has also been used by others to study similar systems,[54–56] including the organic/magnetite interface.[57]

The structures of the ethylenediamine molecules were generated using the AMBERTOOLS package TLEAP, and magnetite slabs terminating with the (100) and (111) surfaces perpendicular to the *x*-axis and approximately 25 Å thick were generated from the pre-relaxed (1 ns of MD simulation at 300 K using the NPT ensemble) bulk structure using the METADISE code.[32] pH was incorporated into the modelling by considering several charged examples of each ethylenediamine molecule and using published pK_a values (Hazardous Substances Data Bank) a weighted average could be determined to reflect the results in the chosen conditions.

Except for the initial relaxation of the bulk structure, the MD simulations were performed using the canonical, NVT, ensemble at 300 K, employing the Nose Hoover thermostat with a relaxation time of 0.5 ps. The trajectories were generated using the Verlet leapfrog algorithm[58] using a time step of 1.0 fs. The long-range coulombic interactions were calculated using the Ewald summation,[59] and the short-range inter- and intramolecular interactions were described using the potential parameters discussed above. Each production run was performed for 5 ns, during which all the atoms within the system were free to relax. The energetics of the system were recorded every 0.1 ps, and the coordinates were written to the general trajectory file every 1 ps. To better scan the configuration space, 42 simulations were run for each molecule on each surface, where the orientation and position of the molecule at the start of the simulation differed. Thus, the results reported represent statistics collected over 210 ns of MD simulation.

Results

Additive screening

When selecting additives for potential future scale-up, it is important to consider the cost. While a compound may be highly effective at face-specific adsorption (such as the MIA protein), if they are not readily available, easily synthesised or competitively priced, the process will not be commercially viable for industrial scale-up. Additives must be water soluble to be effective in green RTCP reactions, and non-toxic. Ethylenediamine is an inexpensive compound, and known to be a chelating agent. Fig. 1a and b schematically shows the setup of the RTCP reactions, and the process of additive-directed synthesis.

We have screened a full ethylenediamine series of H_2N-(–CH_2CH_2N–)$_n$$H_2$ (with n = 2, diethylenetriamine (DETA); 3, triethylenetetramine (TETA); 4, tetraethylenepentamine (TEPA); and 5, pentaethylenehexamine (PEHA)) (Fig. 2b–e) to assess their effectiveness in controlling the morphology of MNPs compared to additive-free control. These additives were selected due to their relatively low cost, the only factor varied in these reactions was the additive used. The amount of additive used per reaction was relative to the number of amine groups present, *i.e.* twice the amount of DETA was used relative to PEHA to maintain 0.08 mmol of active amine groups. As the reaction contained 1 mmol of iron ions, the ratio of functional groups : iron ions was thus 1 : 12.5. As such, the final ratios of additive : iron ions varied depending on the additive used: DETA (1 : 37.5), TETA (1 : 50), TEPA (1 : 62.5), PEHA (1 : 75).

Fig. 2a–e shows representative TEM images of the nanoparticles formed (ESI Fig. S3† for larger TEM images). From visual inspection, it is clear the additives have had a profound effect on particle morphology. The control particles (Fig. 2a) were found to be consistent with previous magnetite MNPs from the literature formed *via* an RTCP route (mean size 22.2 nm, standard deviation (6.5 nm)).[60] The sizes of MNPs from TEM analysis (Fig. 2a–e) and crystallite sizing calculated with the Scherrer equation from the full width maximum of the XRD pattern are in agreement and are shown in Table 1. The addition of the amine additives does not have a significant effect on the MNP/crystallite size and the size distributions are similar for all the reactions with only TETA appearing minimally smaller in size (Fig. 2f, (ESI Fig. S4† for individual histograms)), suggesting that the amine additives do not affect the MNP size.

The XRD patterns (Fig. 2g) of MNPs synthesised with additives are consistent with magnetite being the major crystalline component of each sample (semi-quantitative analysis suggests >80% for all samples). Minor contaminants of other iron oxides (wüstite hematite and maghemite) are present. The control sample contains all 3 contaminants, while small quantities of maghemite and hematite (estimated < 6%) are seen in the reactions mediated by the longer chain PEHA and TEPA additives, and wüstite (estimated < 20%) is seen in the reactions mediated by the short chain DETA and TETA additives. The TEPA mediated sample was found to contain the purest magnetite.

From the analysis of TEM images, the particle shape was assigned (Fig. 2h and 3). Remarkably, the addition of all the ethylenediamine additive resulted in an increased formation of faceted particles (diamond, square, hexagonal). The methodology by which a particle's shape is assigned is demonstrated in Fig. 3 (also see Methods and ESI S2†). It should be noted that TEM images are 2D projections of 3D shapes and as such there can be an overlap and error in the assignment (*e.g.* octahedra commonly project a diamond shape in 2D but can also project hexagonal and square shapes if viewed at a different angle.[41] Similarly, cubes commonly look square but

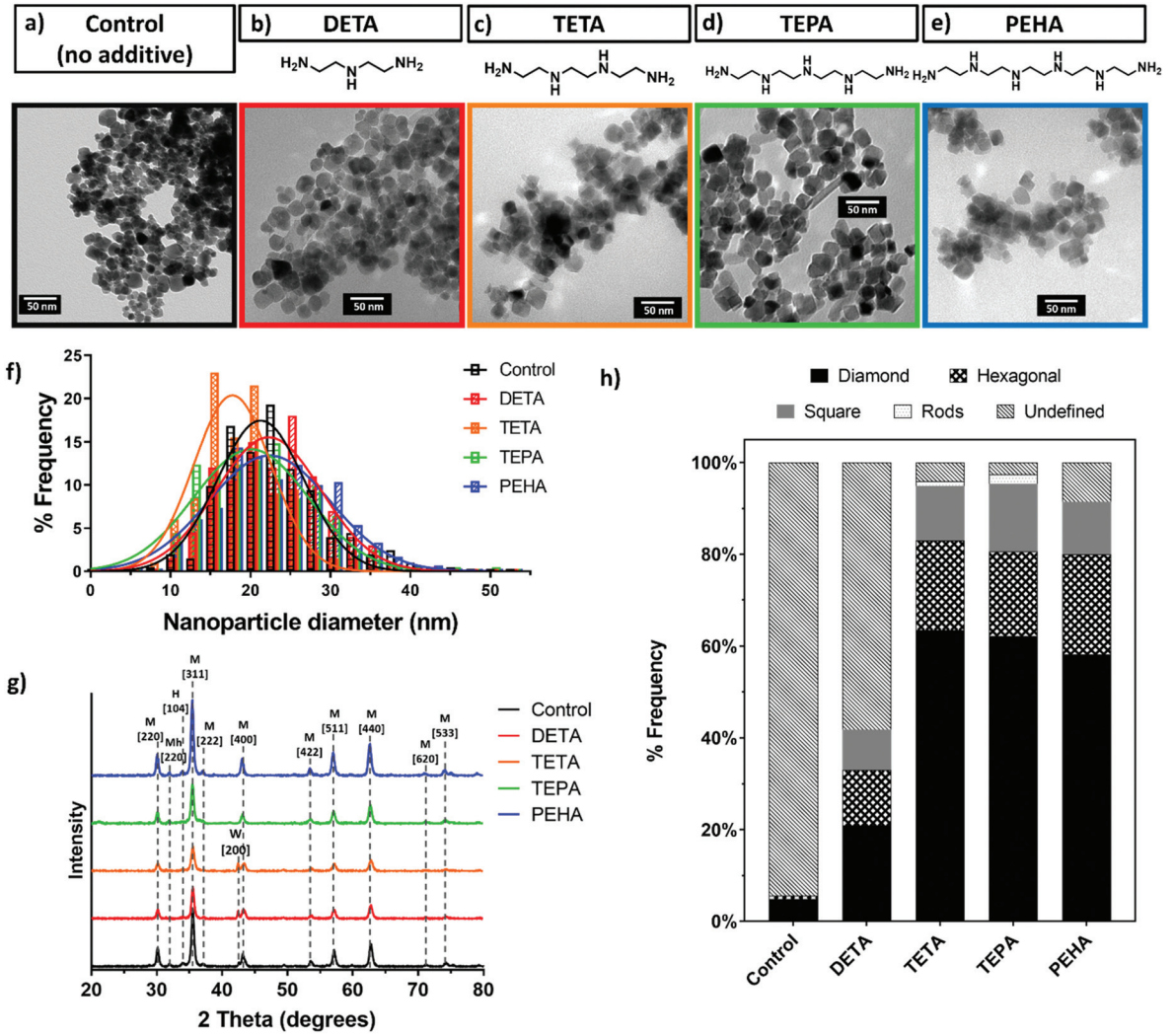

Fig. 2 MNP analysis: Representative TEM images of nanoparticles formed with the addition of various additives. (a) Control (no additive); (b) DETA; (c) TETA; (d) TEPA; (e) PEHA, with scale bars and additive structure. (f) Frequency distribution histogram of particles; (g) annotated XRD data where M = magnetite, Mh = maghemite, H = hematite, and W = wüstite. (h) Shape distribution of particles from TEM images. All scale bars are 50 nm.

Table 1 Table of characterisation of samples from additive screening

Sample	Particle size TEM (nm)	Crystallite size XRD (nm)	% Faceted particles
Control	22.2 ± 6.5	20.4	6
DETA	22.6 ± 6.1	19.3	42
TETA	18.4 ± 5.0	17.5	96
TEPA	23.3 ± 7.2	17.5	97
PEHA	22.9 ± 7.0	18.4	91

can project a hexagon). The populations here show a particular dominance of the octahedral morphology, with mainly diamonds with some square and hexagons. Faceted particles are clearly distinguishable from undefined particles.

A control reaction produced 6% faceted particles, increasing to 42% on addition of DETA, the shortest amine additive tested. The proportion of faceted particles increased with the

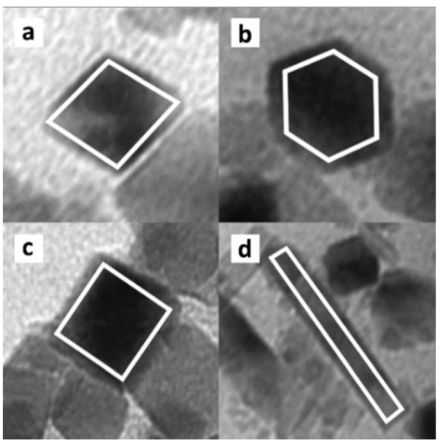

Fig. 3 Sample particle shapes from TEM: (a) diamond, (b) hexagonal, (c) square, and (d) rod.

additive length up to TEPA, with TETA and TEPA producing 96% and 97% of particles with a defined morphology respectively. As the additive chain length increased further for PEHA, 91% of faceted particles were formed. All three TETA, TEPA, and PEHA show highly significant quantities of faceted MNPs with each mediating the production of >60% of diamond particles, assigned to an octahedral morphology. The octahedral nature of these assigned particles was confirmed by the lattice fringe measurement of HRTEM images (Fig. 4). The *d*-spacing of 4.8 Å is indicative of a [111] octahedral plane, confirming a predominantly octahedral morphology in the TEPA additive mediated particle population.

Modelling study

Our previous modelling studies explained why a lysine-rich peptide was able to control the formation of cubic magnetite MNPs by a strong interaction of the amine with the [100] surface of magnetite.[61] In this study we see a series of ethylenediamine molecules of different lengths preferentially mediate the formation of octahedral magnetite MNPs. It is clear the ethylenediamines are not interacting with the [100] and [111] surfaces in the same way as the lysine-rich protein, so again we turned to modelling to explain why these molecules preferentially mediate the formation of octahedral MNPs. We have defined the adsorption energy of the ethylenediamine molecules onto the magnetite surfaces as the difference in the energy of a magnetite slab with an adsorbed molecule and the energy of the same slab and an isolated molecule:[52]

$$E_{\text{ads}} = E_{\text{slab+molecule}} - (E_{\text{slab}} + E_{\text{molecule}})$$

With the exception of DETA, we find the adsorption is endothermic at the [100] surface and exothermic at the [111] surface (Fig. 5), showing a definite preference for the interaction with the [111] face over the [100] face for these molecules. After this quantity has been normalised, to take into to account the varying number of amine groups in the molecule and the overall charge on the molecule, we find that that

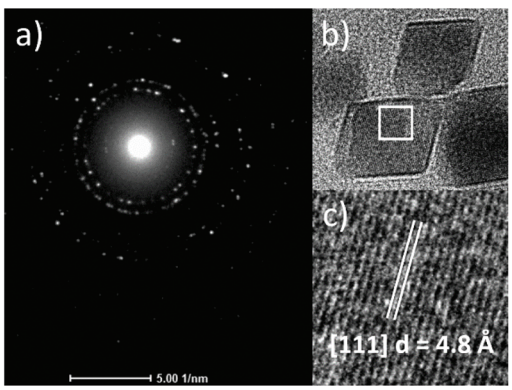

Fig. 4 (a) Selected area electron diffraction of octahedra assigned particles from the TEPA mediated MNP sample, (b) HRTEM of octahedral particles, (c) lattice fringe measurements.

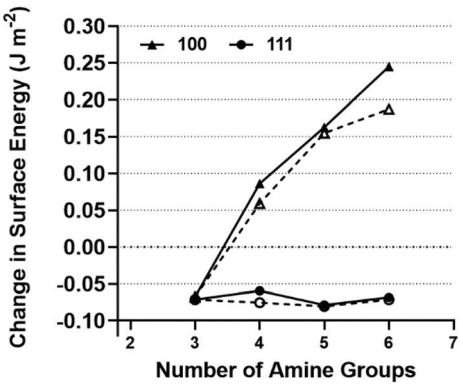

Fig. 5 Calculated changes in the surface energy due to the adsorption polyamine chains of varying lengths. Solid lines at pH 7 and dotted lines at pH 8.

adsorption at the [111] surface is favoured by 100–140 kJ mol^{-1} per unit charge per amine group. There is no significant difference between the calculated values for TETA, TEPA and PEHA but the difference is greater at pH 7 than at pH 8 (Fig. 5).

The surface energy, after adsorption (γ_{ads}), is defined as the difference in energy per unit area between a magnetite slab with an adsorbed molecule and the sum of a bulk system containing the same number of Fe_3O_4 formula units as the slab and an isolated molecule:

$$\gamma_{\text{ads}} = [E_{\text{slab+molecule}} - (E_{\text{bulk}} + E_{\text{molecule}})]/A$$

As a Wulff construction[62] assumes that a crystal will arrange itself such that its surface Gibbs free energy is minimized by assuming a shape of low surface energy the reduction in the energy of a particular surface at the expense of another will be directly related to the observed morphology of the resulting particles. This is shown in Fig. 5 and clearly illustrates that the adsorption of the TETA, TEPA or PEHA molecule leads to a small stabilisation of the [111] surface, whereas adsorption destabilises the [100] surface with the effect increasing with chain length and goes some way to explaining the results shown in Fig. 2h, where octahedral particles are the most abundant when TETA, TEPA and PEHA are present. Note there is negligible difference for both adsorption energies to each magnetite surface and thus less preference for octahedral particles when DETA is present.

The nature of the adsorption, and hence the difference in the calculated surface energies can be understood by considering the nature of the bonding at the surface. This is simply achieved by considering the radial distribution functions (RDF) between the iron and oxygen in the magnetite and the nitrogen and hydrogen atoms in the amine groups. Fig. 6 shows this data for a system at pH 8. The sharp peak at ~1.8 Å in Fig. 6a and c indicates that strong hydrogen bonds form between surface oxygen and the hydrogens in the amine groups for both [100] and [111] surfaces.

As would be expected, the peaks are sharpest for the shortest molecules as there fewer degrees of freedom available

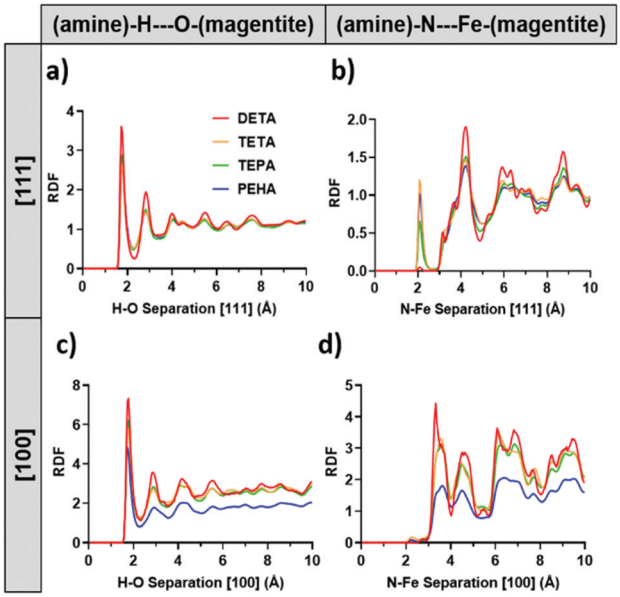

Fig. 6 Radial distribution functions for (a) hydrogen–oxygen interactions and (b) nitrogen–iron interactions at the [111] surface; (c) and (d) show hydrogen–oxygen interactions and nitrogen–iron interactions at the [100] surface.

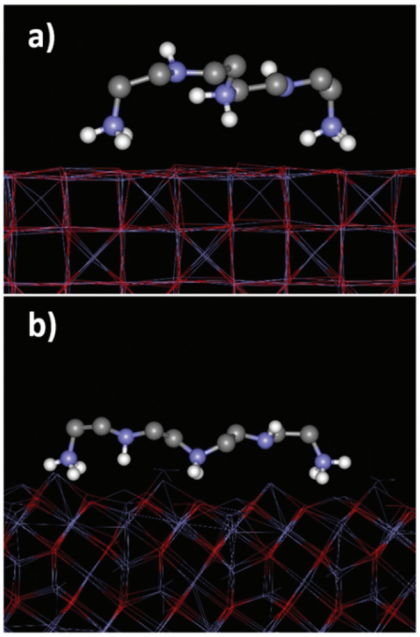

Fig. 7 Atomistic simulations of TEPA interacting with a magnetite surface (a) [100] and (b) with the [111] surface.

during the adsorption and thus the range of bond lengths explored will be smaller. More interesting, and also explaining why the adsorption is stronger at the [111] surface, is the lack of an Fe–N bonding peak at 2 Å in Fig. 6d, which is present in Fig. 6b, illustrating that at the [111] surface both adsorption modes are present, whereas only hydrogen bonding is present at the [100] surface. The link of increased binding with increased binding modes is further demonstrated by the fact the adsorption peak for the Fe–N bonding at [111] is missing only for DETA (Fig. 6b) and DETA shows no difference in surface energy absorption (Fig. 5).

Integrating the first peak of the RDF gives the average number of bonds formed between the adsorbed molecule and the surface.[63] As would be expected, the number of bonds increases with chain length however, more importantly, the number of bonds is significantly greater for the [111] surface than that for [100]. This implies that the longer molecules are better able to lie flat on the [111] surface, forming a stronger interaction with the surface and reducing the surface energy at the [111] surface. Fig. 7 shows PEHA is able to lie flat on the [111] surface (Fig. 7b), which is not the case for the [100] surface (Fig. 7a). Fig. 7b shows additional interactions between surface Fe and the amine groups and N to surface O interactions. However, the data appear to be independent of both chain length and pH for the [111] surface, whereas increasing chain length and reducing pH have a detrimental effect on the [100] surface energy (Fig. 6 and 7).

To further probe the nature of the adsorption, two angular order parameters were defined that describe the orientation of the molecule on the surface.[64] The first is the acute angle formed by a vector, parallel to the surface and a vector connecting the two terminal amine groups and second, the acute angle formed by the vector, parallel to the surface and a vector joining a terminal amine with the centre of mass of the molecule. The results are shown in Table 2.

Table 2 The variation in the angle in degrees between the molecule and the surface. The median value is tabulated with the interquartile range shown in brackets. The numbers are based on the composition of each molecule at pH 8

	End to end	End to centre
	[100]	
DETA	4 (1.8)	28 (4.1)
TETA	20 (26.8)	38 (10.8)
TEPA	24 (24.8)	20 (17.8)
PEHA	45 (32)	29 (29.7)
	[111]	
DETA	15 (18.5)	30 (25.3)
TETA	16 (15.3)	30 (28.4)
TEPA	14 (15)	29 (29.4)
PEHA	15 (15.1)	29 (30.7)

The end–end angle increases steadily with chain length, when considering adsorption at the [100] surface, whereas it remains approximately constant (~15°) when considering adsorption at the [111] surface. With the exception of DETA the angle is always greater for the [100] surface. This, together with variance in the end to centre parameter shows that the molecules are more mobile on the [100] surface, whereas they adsorbed strongly to the [111] surface and remain flat, *i.e.* parallel to surface, further suggesting the molecules' role in promoting the growth of the [111] surface.

Optimising amine additive concentration

The concentration of the additive and thus the ratio of additive to iron ions present in an RTCP reaction is likely to be a critical factor in the effectiveness of MNP control. For this concentration study TEPA was selected owing to it mediating the highest number of faceted particles and the purest magnetite MNPs. 4 different additive : iron ratios were tested, each varying by a factor of 10 (1 : 1250, 1 : 125, 1 : 12.5, 1 : 1.25).

TEM images (Fig. 8a–d) show particles of various sizes and morphologically defined populations (larger images available in ESI Fig. S5†). Fig. 8e and Table 3 (and ESI Fig. S6†) demonstrates that size and size distribution remained consistent at the lower concentrations between the 1 : 1250–1 : 12.5 ratios. At the 1 : 1.25 ratio, there is a significant shift in the profile with respect to both the size and morphology of the particles formed. The mean size of the particles increases from ~22 nm for lower concentrations to 49.4 nm, and the standard deviation increasing from 6.0 to 19.6.

The shape profile (Fig. 8g) shows the particle morphology of the 1 : 1.25 sample to be the poorest too, with 72% of undefined shape (Table 3). It is interesting there are almost equal quantities of diamond and elongated rods (12%) in this poorer 1 : 1.125 sample, showing that high quantities of the additive have a detrimental effect on both the size and morphology. Rod shaped particles are typically associated with the iron oxide goethite, however the XRD (Fig. 8f) shows that for each sample magnetite is the main crystalline product, with only a small quantity of goethite impurity in all samples. In fact, the XRD data remained consistent between all the samples, suggesting the difference in particle morphology is not the result of different iron oxides species being present.

The ratio 1 : 125 was found to produce the most consistently faceted particles, with 81% of the particles formed being faceted with >70% being octahedral (Table 3). The ratios above and below, (1 : 1250 and 1 : 12.5 respectively) display a similar size and shape profile to each other. 1 : 125 TEPA : Fe ratio showing the best shape control is consistent with the previous additive screening results. The initial screening used a concentration of 1 : 62.5 (twice the concentration of 1 : 125, and between 1 : 125 and 1 : 12.5 values). It is interesting to note that the optimum proportion of faceted particles is actually achieved in the initial screening, but this concentration study achieves a more morphologically consistent diamond-shaped population.

To better understand if and when TEPA is binding to the forming particles, FT-IR spectroscopy was performed at a range of pH from 4.5 to 12.8 (ESI Fig. S6†). The magnetite particles give a strong Fe–O peak at 542 cm^{-1} (and a minor one at 691 cm^{-1}). The signal from an amine organic coating (bending frequencies occurring between 1220 and 1747 cm^{-1}) is the most predominant in pH 7.4 and pH 9 samples while only a negligible signal is seen in the extreme pH values of 4.5 and 12.8. This suggests TEPA binds only after the particle has nucleated (above pH 4.5), thus to the surface as opposed to iron ions. Above pH 12, TEPA is exclusively neutral with no

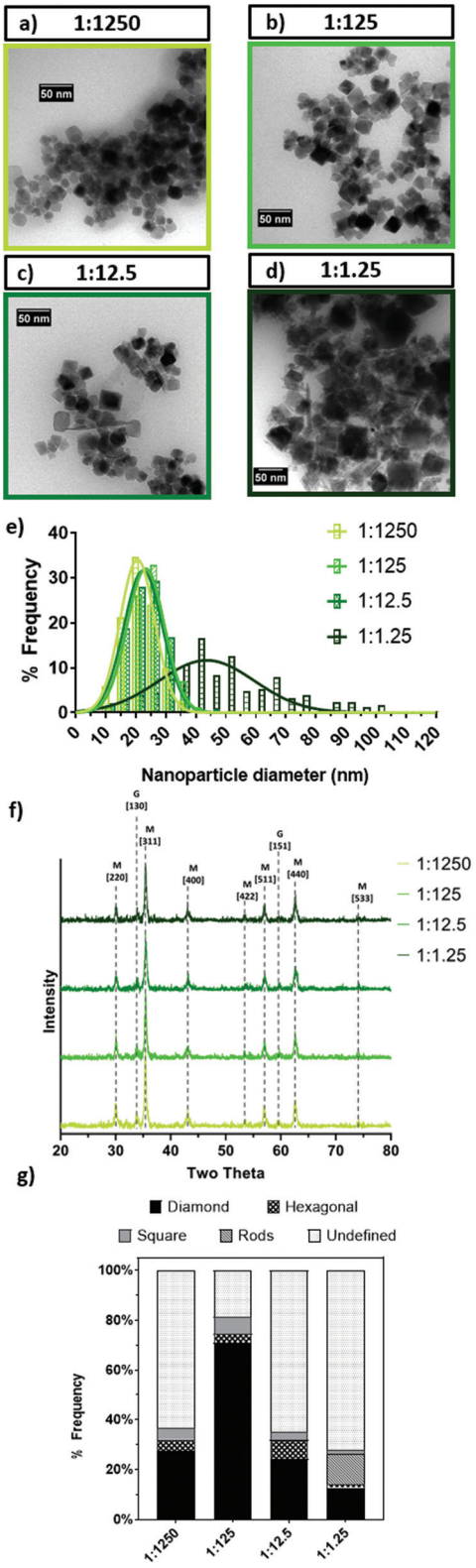

Fig. 8 MNP analysis: Representative TEM images of nanoparticles formed with varying TEPA : iron ion ratios. (a) 1 : 1250; (b) 1 : 125; (c) 1 : 12.5; (d) 1 : 1.25; (e) frequency distribution histogram of particles; (f) annotated XRD data where M = magnetite and G = goethite; (g) shape distribution of particles from TEM images. All scale bars are 50 nm.

Table 3 Table of characterisation of samples from the concentration study

Sample TEPA : Fe	Particle size TEM (nm)	Crystallite size XRD (nm)	% Faceted particles (total)			
			Diamond	Hexagonal	Square	Rod
1 : 1250	21.1 ± 6.0	23.0	*37*			
			28	5	5	—
1 : 125	23.5 ± 6.0	24.0	81			
			71	3	7	—
1 : 12.5	22.7 ± 6.0	26.2	35			
			24	7	3	1
1 : 1.25	49.4 ± 19.6	23.0	*28*			
			13	1	2	12

$-NH_3^+$ or $-NH_2-^+$ groups for electrostatic interaction, suggesting the TEPA completely disassociates from the particles at above pH 12. TGA (ESI Fig. S6†) suggests the presence of TEPA as an organic coating at pH7.

Discussion

RTCP is a simple, well-studied method of producing large quantities of magnetite nanoparticles, with the drawback that particles produced have an undefined morphology. While a range of natural additives have being used in an RTCP reaction to control the MNP size, the use of biomineralisation proteins and peptides to control both the size and shape as well as produce higher quality particles is well documented,[38,60,65,66] with varied complexities and functionalities. A molecule that specifically adsorbs to a developing crystal face, reduces its surface energy to slow the growth of the face, resulting in that facet dominating the final morphology of the crystal.[38] Peptide and protein control over nanoparticle morphology has been ascribed to precise mapping of the specific surface resulting in multiple interactions. In this study we used the learning from such proteins. They were found to be lysine-rich showing strong amine interactions with the magnetite surface.

EDA is an inexpensive, simple, amine compound and has previously been used as well as DETA as a structure-directing agent (in non-green synthetic conditions).[67,68] The addition of EDA based additives of all lengths tested (amine groups = 3–6, DETA–PEHA) had an influence on the morphology of the particles, with an increased percentage of faceted particles being observed from DETA to TETA, with TETA to PEHA showing close to pure faceted particles (optimum found at TEPA). Particle size remained consistent (~18–23 nm) between samples synthesised with no additive and the samples produced with all additives, suggesting the additive does not play a role in nucleating the MNPs. This is to be expected as mineral nucleation is usually facilitated by acidic proteins in biomineralisation (containing multiple aspartic and glutamic acid) providing sites for metal ion binding.[21] An additive that affects nucleation will generally influence the mineral type and/or the particle size, neither of which is seen here. Instead the amine molecules exclusively act to control morphology, preferentially adsorbing to and stabilising the [111] face to direct the growth of [111] faceted octahedral particles. This is consistent with what is currently understood in the literature and from our modelling studies.[29]

Production of octahedral MNPs *via* a green additive synthesis is a very important advance for biomedicine. Such faceted particles are very desirable for both therapeutics and diagnostic nanomedicine, while cheap sustainable manufacture will increase accessibility leading to more widespread uses. While it is clear the EDA series of additives primarily acts to direct the morphology of the growing crystal, in doing so the amine chains bind to the surface. This has a secondary feature of forming an organic coating. This helps to stabilise and increase the dispersion of the MNPs in solution. The amine additives could thus be modified to also functionalise the particles if desired, giving the additive a dual purpose. However, the additive does not bind at extreme pH, so can be easily removed with base by continuing the titration if desired.

It is clear from the additive screening that TETA, TEPA and PEHA produce the majority octahedral particles (while DETA is less effective). Computational simulation studies explain why the ethylenediamine series directs the morphology towards octahedral particles. The modelling demonstrates a clear preferential binding to the [111] face over the [100]. Despite the identical functional groups, additive performance is affected by their length, with the shortest DETA showing only a minor effect. While TETA, TEPA, and PEHA are comparable, there is a slight reduction in performance from PEHA, the longest amine molecule. From the modelling data we see DETA shows no preference for [111] or [100] and this explains why it had the least influence over particle morphology.

Modelling also shows the energies of absorption for binding are similar for TETA, TEPA and PEHA for both the [111] and [100] magnetite surfaces. This seems to be driven by a mixture of the positive effect of chelation coupled with the negative effect of entropy for long molecules which may explain the slight fall off for PEHA. The adsorption at the [111] surface is favoured by TETA, TEPA and PEHA because the arrangement of the ions on the surface enables the molecule to adsorb flat and form, not only hydrogen bonds between the magnetite surface oxygen and hydrogens on the amine groups, but also strong interactions between surface iron and nitrogen groups in the amine. Whereas only hydrogen bonding is able to occur at the [100] surface and to a lesser extent to that pre-

dicted at the [111] surface. It should be noted that the energy changes required to favour one surface over the other can be small, thus subtle changes in the form of the additive molecule result in a substantial effect to the MNP morphology. For example, it is noteworthy that the ethylenediamine series was inspired by the basic amino acid rich morphology controlling protein, with a particularly high quantity of lysine. The lysine rich peptide loop directed magnetite MNP morphology towards cubic particles, showing a preference to the [100] face. It is interesting that because these seemingly similar molecules (differ by a carboxylate group) bind differently to the magnetite [111] and [100] surfaces, a dramatically different morphological outcome is achieved. This is something that, carefully designed, computer modelling can probe as the techniques are able to directly compare adsorption at different surfaces and consider a variety of adsorption modes.

From varying the concentration of TEPA by factors of 10, a rough ideal concentration was ascertained as ~1 : 125. This is in line with the results seen for the screening which used a 1 : 62.5 ratio. At 1 : 1250 and 1 : 12.5, similar degrees of morphological control were exerted over the MNP formed, despite the difference in conditions. This may be because below the ideal concentration there may be too little of the additive for surface coverage to have a substantial effect on particle formation, and at high concentrations the reaction conditions such as pH may be altered by the additive, effectively polluting the reaction environment. This seems to be the case at near 1 : 1 additive to iron concentrations. This study was conceived to translate a green bioinspired approach to scale-up. A chief concern with scale is cost. This study demonstrates a vastly cheaper additive compared to protein alternatives and the concentration study reveals that very small quantities of this cheap additive (1 : 125) are the optimum, which is a very positive news for scale-up.

Conclusions

Ethylenediamine based additives have been successfully used to enhance magnetite MNPs formed under a high-yielding, environmentally friendly RTCP, by directing the formation of octahedral particles. A modelling study revealed that the longer EDA series molecules adsorb strongly and lie flatter against a [111] octahedral magnetite surface; conversely adsorption to a [100] surface is unfavourable. As such both modelling and experimental results align to represent the potency of the longer EDA molecules (TETA, TEPA, PEHA) as shape-directing additives for octahedral magnetite. Only a small quantity of the additive is required to offer optimum control. This study realises and explains the power of the bioinspired-additive green chemistry approach to MNP synthesis. Previous work has demonstrated how metal-alloy nanoparticle phase,[69] silica mesoporosity,[70] and morphology of many nanoparticles such as magnetite,[43] calcite,[71] and platinum[72] can be controlled using proteins and peptides in similar simple green precipitation reactions. Learning from biology, here we have used only the specific functionalities and motifs on simpler organic molecular additives. We demonstrated that easily accessible additives can define and control the MNP morphology. More widely, this methodology has the potential to translate to a full range of nanomaterials, most readily those where protein/peptide directed synthesis has already been demonstrated, with a scalable universal green nanomaterial synthesis offering a huge impact for nanomaterial manufacture.

Abbreviations

DETA	Diethylenetriamine
EDA	Ethylenediamine
FCC	Face-centred cubic
FTIR	Fourier-transform infrared spectroscopy
FWHM	Full width half maximum
HRTEM	High resolution transmission electron microscopy
MIA	Magnetite interacting adhiron
Mms	Magnetosome membrane specific
MNP	Magnetic nanoparticle
MRI	Magnetic resonance imaging
NaOH	Sodium hydroxide
PEHA	Pentaethylenehexamine
RDF	Radial distribution functions
RTCP	Room temperature co-precipitation
TEM	Transmission electron microscopy
TETA	Triethylenetetramine
TGA	Thermal gravimetric analysis
TEPA	Tetraethylenepentamine
VSM	Vibrating sample magnetometry
XRD	X-ray powder diffraction

Conflicts of interest

There are no conflicts of interest to declare.

Acknowledgements

This work was supported by funding from the EPSRC (grant number EP/P006892/1) and the University of Sheffield's ESPRC DTP allowance (grant number EP/M508135/1) funds Laura Norfolk's PhD. The research was supported by David Cooke's membership of the UK's HEC Materials Chemistry Consortium, funded by the EPSRC (EP/L000202, EP/R029431), and used THOMAS, the UK Materials and Molecular Modelling Hub, for computational resources, which is partially funded by the EPSRC (EP/P020194). We thank S. Tsokov and C. Hill (Sheffield Electron Microscopy unit) for TEM training and HRTEM, Nicola Morley and Zhao Leong for support with VSM and Craig Robertson for support with powder XRD.

Notes and references

1 R. E. Rosensweig, *Sci. Am*, 1982, pp. 136–145.
2 E. Y. M. Mendoza, A. S. Santos, E. V. López, V. Drozd, A. Durygin, J. Chen and S. K. Saxena, *J. Mater. Res. Technol.*, 2019, **8**, 2944–2956.
3 B. Issa, I. M. Obaidat, B. A. Albiss and Y. Haik, *Int. J. Mol. Sci.*, 2013, **14**, 21266–21305.
4 C. Y. Haw, F. Mohamed, C. H. Chia, S. Radiman, S. Zakaria, N. M. Huang and H. N. Lim, *Ceram. Int.*, 2010, **36**, 1417–1422.
5 M. Mahdavi, M. Bin Ahmad, M. J. Haron, F. Namvar, B. Nadi, M. Z. Ab Rahman and J. Amin, *Molecules*, 2013, **18**, 7533–7548.
6 K. Mahmoudi, A. Bouras, D. Bozec, R. Ivkov and C. Hadjipanayis, *Int. J. Hyperthermia*, 2018, 1–13.
7 P. Sharma, S. Brown, G. Walter, S. Santra and B. Moudgil, *Adv. Colloid Interface Sci.*, 2006, **123**, 471–485.
8 M. Gaumet, A. Vargas, R. Gurny and F. Delie, *Eur. J. Pharm. Biopharm.*, 2008, **69**, 1–9.
9 J. Motoyama, T. Hakata, R. Kato, N. Yamashita, T. Morino, T. Kobayashi and H. Honda, *Biomagn. Res. Technol.*, 2008, **6**, 1–9.
10 M. Gonzales-Weimuller, M. Zeisberger and K. M. Krishnan, *J. Magn. Magn. Mater.*, 2009, **321**, 1947–1950.
11 L. Zhang, R. He and H. C. Gu, *Mater. Res. Bull.*, 2006, **41**, 260–267.
12 D. Santos-Carballal, A. Roldan, R. Grau-Crespo and N. H. de Leeuw, *Phys. Chem. Chem. Phys.*, 2014, **16**, 21082–21097.
13 G. Zhen, B. W. Muir, B. a. Moffat, P. Harbour, K. S. Murray, B. Moubaraki, K. Suzuki, I. Madsen, N. Agron-Olshina, L. Waddington, P. Mulvaney and P. G. Hartley, *J. Phys. Chem. C*, 2011, **115**, 327–334.
14 A. Nikitin, M. Fedorova, V. Naumenko, I. Shchetinin, M. Abakumov, A. Erofeev, P. Gorelkin, G. Meshkov, E. Beloglazkina, Y. Ivanenkov, N. Klyachko, Y. Golovin, A. Savchenko and A. Majouga, *J. Magn. Magn. Mater.*, 2017, **441**, 6–13.
15 P. Hugounenq, M. Levy, D. Alloyeau, L. Lartigue, E. Dubois, V. Cabuil, C. Ricolleau, S. Roux, C. Wilhelm, F. Gazeau and R. Bazzi, *J. Phys. Chem. C*, 2012, **116**, 15702–15712.
16 S. K. Shaw, A. Biswas, A. Gangwar, P. Maiti, C. L. Prajapat, S. Singh and N. K. Prasad, *J. Magn. Magn. Mater.*, 2019, **484**, 437–444.
17 C. H. Ho, C. P. Tsai, C. C. Chung, C. Y. Tsai, F. R. Chen, H. J. Lin and C. H. Lai, *Chem. Mater.*, 2011, **23**, 1753–1760.
18 L. Zhang, Q. Li, S. Liu, M. Ang, M. O. Tade and H. C. Gu, *Adv. Powder Technol.*, 2011, **22**, 532–536.
19 P. Hugounenq, M. Levy, D. Alloyeau, L. Lartigue, E. Dubois, V. Cabuil, C. Ricolleau, S. Roux, C. Wilhelm, F. Gazeau and R. Bazzi, *J. Phys. Chem. C*, 2012, **116**, 15702–15712.
20 A. G. Roca, L. Gutiérrez, H. Gavilán, M. E. Fortes Brollo, S. Veintemillas-Verdaguer and M. del P. Morales, *Adv. Drug Delivery Rev.*, 2019, **138**, 68–104.
21 M. C. Mascolo, Y. Pei and T. A. Ring, *Materials*, 2013, **6**, 5549–5567.
22 A. Abou Hassan, O. Sandre, V. Cabuil and P. Tabeling, *Chem. Commun.*, 2008, 1783–1785.
23 L. Norfolk, A. E. Rawlings, J. P. Bramble, K. Ward, N. Francis, R. Waller, A. Bailey and S. S. Staniland, *Nanomaterials*, 2019, **9**, 1729.
24 Â. L. Andrade, D. M. Souza, M. C. Pereira, J. D. Fabris and R. Z. Domingues, *Quím. Nova*, 2010, **33**, 524–527.
25 S. Si, A. Kotal, T. K. Mandal, S. Giri, H. Nakamura and T. Kohara, *Chem. Mater.*, 2004, **16**, 3489–3496.
26 S. Wan, J. Huang, H. Yan and K. Liu, *J. Mater. Chem.*, 2006, **16**, 298–303.
27 Y. P. Yew, K. Shameli, M. Miyake, N. Kuwano, N. B. Bt Ahmad Khairudin, S. E. Bt Mohamad and K. X. Lee, *Nanoscale Res. Lett.*, 2016, **11**, 1–7.
28 V. V. Makarov, A. J. Love, O. V. Sinitsyna, S. S. Makarova, I. V. Yaminsky, M. E. Taliansky and N. O. Kalinina, *Acta Nat.*, 2014, **6**, 35–44.
29 I. P. Sari and Y. Yulizar, *IOP Conf. Ser.: Mater. Sci. Eng.*, 2017, **191**, 1–5.
30 N. M. Salem and A. M. Awwad, *Nanosci. Nanotechnol.*, 2013, **3**, 35–39.
31 V. L. Kirillov, D. A. Balaev, S. V. Semenov, K. A. Shaikhutdinov and O. N. Martyanov, *Mater. Chem. Phys.*, 2014, **145**, 75–81.
32 Y. Kuwahara, T. Miyazaki, Y. Shirosaki, G. Liu and M. Kawashita, *Ceram. Int.*, 2016, **42**, 6000–6004.
33 W. L. Tan and M. A. Bakar, *J. Phys. Sci.*, 2006, **17**, 37–50.
34 B. Yang, J. Chou, X. Dong, C. Qu, Q. Yu, K. J. Lee and N. Harvey, *J. Phys. Chem. C*, 2017, **121**, 8961–8967.
35 A. Kora, S. Beedu and A. Jayaraman, *Org. Med. Chem. Lett.*, 2012, **2**, 17.
36 S. Wei, Y. Wang, Z. Tang, J. Hu, R. Su, J. Lin, T. Zhou, H. Guo, N. Wang and R. Xu, *New J. Chem.*, 2020, **44**, 9304–9312.
37 A. Arakaki, J. Webb and T. Matsunaga, *J. Biol. Chem.*, 2003, **278**, 8745–8750.
38 S. S. Staniland and A. E. Rawlings, *Biochem. Soc. Trans.*, 2016, **44**, 883–890.
39 M. Tanaka, E. Mazuyama, A. Arakaki and T. Matsunaga, *J. Biol. Chem.*, 2011, **286**, 6386–6392.
40 L. Wang, T. Prozorov, P. E. Palo, X. Liu, D. Vaknin, R. Prozorov, S. Mallapragada and M. Nilsen-Hamilton, *Biomacromolecules*, 2012, **13**, 98–105.
41 S. S. S. Johanna, M. Galloway, A. Arakaki, F. Masuda, T. Tanaka and T. Matsunaga, *J. Mater. Chem.*, 2011, **21**, 15244–15254.
42 A. E. Rawlings, J. P. Bramble, R. Walker, J. Bain, J. M. Galloway and S. S. Staniland, *Proc. Natl. Acad. Sci. U. S. A.*, 2014, **111**, 16094–16099.
43 A. E. Rawlings, J. P. Bramble, A. A. S. Tang, L. A. Somner, A. E. Monnington, D. J. Cooke, M. J. McPherson, D. C. Tomlinson and S. S. Staniland, *Chem. Sci.*, 2015, **6**, 5586–5594.

44 UK-Peptides, Buy IGF1 LR3, https://www.uk-peptides.com/igf1-lr3-1mg.
45 Merck, Tetraethylenepentamine, https://www.sigmaaldrich.com/catalog/product/aldrich/t11509?lang=en&region=GB.
46 W. Smith and T. R. Forester, *J. Mol. Graphics*, 1996, **7855**, 136–141.
47 J. Wang, R. M. Wolf, J. W. Caldwell, P. A. Kollman and D. A. Case, *J. Comput. Chem.*, 2004, **25**(9), 1157–1174.
48 R. T. Cygan, J. Liang and A. G. Kalinichev, *J. Phys. Chem. B*, 2004, **108**(4), 1255–1266.
49 S. Kerisit, *Geochim. Cosmochim. Acta*, 2011, **75**, 2043–2061.
50 H. A. Lorentz, *Ann. Phys.*, 1881, **248**, 127–136.
51 D. Berthelot, *C. R. Hebd. des séances l'Acad. des Sci.*, 1898, **126**, 1703–1855.
52 J. H. Harding and D. M. Duffy, *J. Mater. Chem.*, 2006, **16**, 1105–1112.
53 A. Monnington, *Magnetite Biomineralisation: The Interactions of Proteins and Fe_3O_4 Surfaces*, Phd Thesis, University of Huddersfield, 2014.
54 M. Szczerba and A. G. Kalinichev, *Clays Clay Miner.*, 2016, **64**, 488–502.
55 T. V. Shapley, M. Molinari, R. Zhu and S. C. Parker, *J. Phys. Chem. C*, 2013, **117**, 24975–24984.
56 J. A. Greathouse, D. B. Hart, G. M. Bowers, R. J. Kirkpatrick and R. T. Cygan, *J. Phys. Chem. C*, 2015, **119**, 17126–17136.
57 M. Konuk, K. Sellschopp, G. B. Vonbun-Feldbauer and R. H. Meißner, *J. Phys. Chem. C*, 2021, 4794–4805.
58 L. Verlet, *J. Phys. Chem. C*, 1967, **125**, 4794–4805.
59 P. P. Ewald, *Ann. Phys.*, 1921, **369**, 253–287.
60 A. E. Rawlings, L. A. Somner, M. Fitzpatrick-Milton, T. P. Roebuck, C. Gwyn, P. Liravi, V. Seville, T. J. Neal, O. O. Mykhaylyk, S. A. Baldwin and S. S. Staniland, *Nat. Commun.*, 2019, 2873.
61 A. E. Rawlings, J. P. Bramble, A. A. S. Tang, L. A. Somner, A. E. Monnington, D. J. Cooke, M. J. McPherson, D. C. Tomlinson and S. S. Staniland, *Chem. Sci.*, 2015, **6**, 5586–5594.
62 G. Wulff, *Z. Kristallogr. Mineral.*, 1901, **34**, 449–530.
63 M. P. Allen and D. J. Tildesley, *Computer Simulation of Liquids*, Oxford University Press, Oxford, 1st edn, 1987.
64 D. J. Cooke and J. A. Elliott, *J. Chem. Phys.*, 2007, **127**, 1–10.
65 R. Lopez-Moreno, A. Fernández-Vivas, C. Valverde-Tercedor, A. I. Azuaga Fortes, S. Casares Atienza, A. B. Rodriguez-Navarro, R. Zarivach and C. Jimenez-Lopez, *Cryst. Growth Des.*, 2017, **17**, 1620–1629.
66 J. J. M. Lenders, H. R. Zope, A. Yamagishi, P. H. H. Bomans, A. Arakaki, A. Kros, G. De With and N. A. J. M. Sommerdijk, *Adv. Funct. Mater.*, 2015, **25**, 711–719.
67 D. Arndt, V. Zielasek, W. Dreher and M. Bäumer, *J. Colloid Interface Sci.*, 2014, **417**, 188–198.
68 D. Zhang, J. Zheng and Z. Tong, *J. Exp. Nanosci.*, 2010, **5**, 162–168.
69 R. M. Jarrald, A. W. Liang Alvin, A. E. Rawlings, M. Tanaka, M. Okochi and S. S. Staniland, *Bioconjugate Chem.*, 2020, **31**, 1981–1994.
70 D. J. Belton, S. V. Patwardhan and C. C. Perry, *J. Mater. Chem.*, 2005, **15**, 4629–4638.
71 D. B. DeOliveira and R. A. Laursen, *J. Am. Chem. Soc.*, 1997, **7863**, 10627–10631.
72 C. Y. Chiu, Y. Li, L. Ruan, X. Ye, C. B. Murray and Y. Huang, *Nat. Chem.*, 2011, **3**, 393–399.